Journal Pre-proofs

Article

High interfacial-energy heterostructure facilitates large-sized lithium nucleation and rapid Li^+ desolvation process

Zhipeng Wen, Yuanhong Kang, Qilong Wu, Xiu Shen, Pengbin Lai, Yang Yang, Cheng Chao Li, Jinbao Zhao

PII: S2095-9273(22)00546-1
DOI: https://doi.org/10.1016/j.scib.2022.11.026
Reference: SCIB 1946

To appear in: *Science Bulletin*

Received Date: 8 October 2022
Revised Date: 8 November 2022
Accepted Date: 14 November 2022

Please cite this article as: Z. Wen, Y. Kang, Q. Wu, X. Shen, P. Lai, Y. Yang, C.C. Li, J. Zhao, High interfacial-energy heterostructure facilitates large-sized lithium nucleation and rapid Li^+ desolvation process, *Science Bulletin* (2022), doi: https://doi.org/10.1016/j.scib.2022.11.026

This is a PDF file of an article that has undergone enhancements after acceptance, such as the addition of a cover page and metadata, and formatting for readability, but it is not yet the definitive version of record. This version will undergo additional copyediting, typesetting and review before it is published in its final form, but we are providing this version to give early visibility of the article. Please note that, during the production process, errors may be discovered which could affect the content, and all legal disclaimers that apply to the journal pertain.

Received 8-October-2022; Revised 8-November-2022; Accepted 14-November-2022

High interfacial-energy heterostructure facilitates large-sized lithium nucleation and rapid Li^+ desolvation process

Zhipeng Wen[1,2], Yuanhong Kang[2], Qilong Wu[2], Xiu Shen[2], Pengbin Lai[2], Yang Yang[2*], Cheng Chao Li[1*], Jinbao Zhao[2]*

[1] School of Chemical Engineering and Light Industry, Guangdong University of Technology, Guangzhou 510006, China

[2] State Key Lab of Physical Chemistry of Solid Surfaces, Collaborative Innovation Centre of Chemistry for Energy Materials, State-Province Joint Engineering Laboratory of Power Source Technology for New Energy Vehicle, Engineering Research Center of Electrochemical Technology, Ministry of Education, College of Chemistry and Chemical Engineering, Xiamen University, Xiamen 361005, China.

* Corresponding authors. E-mail: yangyang419@xmu.edu.cn (Y. Yang); licc@gdut.edu.cn (C. C. Li); jbzhao@xmu.edu.cn (J. Zhao)

Abstract: High interfacial energy Li^0-electrolyte interface contributes to larger Li^0 nucleation embryos and a more stable interface, so the interfacial energy is essential for highly reversible Li^0 deposition/stripping. Herein, a high interfacial-energy artificial solid electrolyte interphase

Journal Pre-proofs

(SEI) with rich LiF embedded in lithiated poly-2-acrylamido-2-methylpropane sulfonic acid (PAMPS-Li) network is designed to realize favorable Li^0 nucleation and rapid desolvation of Li^+ simultaneously. The Li−F bonds in LiF (001) exhibit stronger ion-dipole interactions with Li atoms, offering higher interfacial energies. When the growth surface energy and total interfacial energy of Li^0 are balanced, the high interfacial energy SEI with abundant LiF can promote the formation of larger Li^0 nucleation embryos. In addition, the PAMPS-Li with immobilized anions presents weaker interaction with Li^0 and possesses higher polymer-Li interfacial energy, and its amide and sulfonic acid groups exhibit higher binding energies with Li^+. Therefore, PAMPS-Li can easily promote the Li^+ to escape from the solvent sheath and weaken the desolvation energy barrier. The highly reversible Li^0 deposition behavior with restricted side reactions is achieved based on the synergistic modification of high interfacial energy SEI with heterostructure. Most importantly, lifespan of multi-layered Li^0 pouch cell (330 Wh kg^{-1}) with a low N/P ratio (1.67) is over 100 cycles, verifying its potential practical application.

Keywords: crystalline LiF-rich, high interfacial energy, large metallic Li^0 nucleate size, rapid Li^+ desolvation, pouch cell

1. Introduction

Compared to commercial lithium-ion batteries, metallic Li^0 batteries offer higher mass-specific capacity (3860 mAh g^{-1}) and can be coupled with alternative conversion-type cathodes with high capacity [1-3]. As they may realize higher energy density, metallic Li^0 batteries is attracting considerable critical attention, buts their application is stymied by short lifespan and low coulombic efficiency. Generally, lifespan shortfall is essentially resulted from accumulation of

inactive (called 'dead') Li during cycling, which is composed of both (electro)chemically produced Li^+ components in the solid electrolyte interphase (SEI) and electrically isolated unreacted metallic Li^0 [4].

Various strategies have been proposed to enhance the Li^0 plating/stripping reversibility, including electrolyte formulation [5], artificial protective layer construction [6], deposition substrate design [7,9], and charge-discharge reconfiguration [10, 11]. Most recent studies focus on stabilizing the electrode/electrolyte interface, which is the primary electrochemical reaction site. For the metallic Li^0/electrolyte interphase, the intrinsic features of SEI are strongly associated with the metallic Li^0 deposition. Firstly, the SEI constituent plays a crucial role in regulating the flatness, dispersion, and size of metallic Li^0 nucleation. Besides, high mechanical strength and good (electro)chemical stability are vital for ideal SEI. Uncontrolled growth of metallic Li^0 dendrites breaks the brittle SEI, which consumes the electrolyte and active Li^0 via irreversible side reactions, resulting in rapid fading of battery capacity. Fluorinated SEI has emerged as a preferred option in recent years, which can regulate the Li-deposition behaviors and prolong the lifespan of metallic Li^0 batteries. The fluorinated SEI contains high level of LiF, which is accepted as its central feature. The grain boundaries within LiF promotes the smooth motion of Li^+ inside the SEI, facilitating the flat deposition of metallic Li^0. However, many fabrication methods of fluorinated SEI, including skeleton of soybean protein fiber [12], lithiophilic hybrid Janus interphase [13], spray quenching on molten Li [14], and self-assembled monolayers modified separator [15], show complex process and questionable feasibility in high-loading mass pouch cells. It should be noted that organic components of SEI (RCOLi, R=CH_2, CH_2CH_3, etc.) are also generated during the cycling [16, 17], but their targeted modification and regulation are usually overlooked when the traditional fluorinated SEI is adopted. They, in

commercial carbonate-based electrolytes, are mainly derived from degradation of electrolyte and Li, which are extremely limited in relieving the volume expansion of Li^0 plating. In addition, their poor property in Li^+ transition dramatically deteriorates the formation of SEI film.

The solvated Li^+ initially exfoliates the solvated sheaths at the SEI-electrolyte solid-liquid interface to analyze the Li^0 deposition fundamentally. Then, the naked Li^+ accepts electrons at the bulk Li/SEI solid-solid interphase, and Li^0 nucleation occurs on the metallic Li^0 surface or current collector. Furthermore, Li^+ flux in the SEI layer replenishes the ions near the Li^0 core and promotes further deposition and growth of Li^0 [18]. Therefore, Li^+ desolvation, Li^0 nucleation, and Li^+ flow are equally significant for Li^0 deposition. An ideal SEI interfacial layer not only requires excellent chemical/electrochemical stability but also exerts a synergistic effect in manipulating the above three processes.

After in-depth analysis on the Li^0 deposition behavior, a multifunctional artificial SEI is designed, which can simultaneously realize rapid desolvation of Li^+ and regulate Li^0 deposition on commercial Li^0 foil using a facile and fast spraying method. The SEI with heterostructure mainly consists of crystalline LiFs derived from in-situ lithiation of fluorinated carbon nanotubes (FCNTs) and cross-crosslinked single-ion conductor (lithiated poly-2-acrylamido-2-methylpropane sulfonic acid, PAMPS-Li). In the solvent environment near to the metallic Li^0 interface, the solvated Li^+ exhibits stronger binding energy with PAMPS-Li, which is favorable for desolvation. The cross-linked PAMPS-Li forms a network structure inside the SEI, creating Li^+ ion channels and ensuring consistent Li^+ flow (Fig. 1a). Finally, the crystalline LiF exhibits higher interfacial energy with Li, forming a larger limit size to promote the metallic Li^0 deposition (Fig. 1b). Practically, this method is easily employed to large-scale roll-to-roll mass

process. As a proof of concept, 330 wh kg^{-1} metallic Li^0 pouch cell is performed for 100 stable cycles with a low N/P ratio of 1.67.

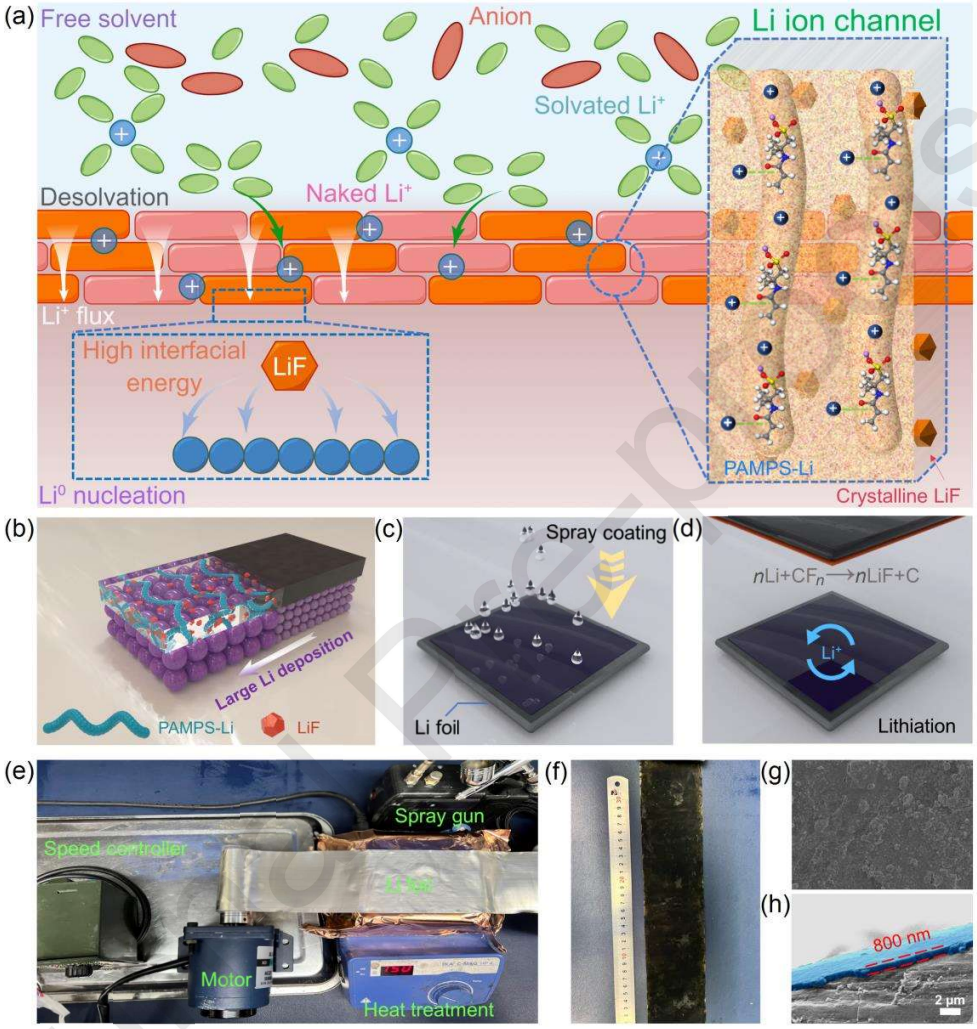

Fig. 1. (Color online) The function in metallic Li^0 deposition and characterization of FCNTs@Li. (a) The schematic illustration for the roles of FCNTs@Li in metallic Li^0 deposition. (b) The structure sketch map of FCNTs@Li during cycling. (c) and (d) The schematic illustration of fabrication and lithiation of FCNTs@Li, respectively. (e) and (f) The optical image of large-scale fabrication of FCNTs@Li system and sample, respectively. (g) and (h) The front-section and cross-section scanning electron microscope (SEM) images of FCNTs@Li, respectively.

2. Experimental

2.1 Preparation of FCNTs@Li anode

Typically, 0.02 g FCNTs, 0.009 g PAMPS-Li, and 0.001 g poly(vinylidene fluoride) (PVDF) were dissolved in 10 mL of *N*-methylpyrrolidone (NMP). Then, the mixed solvent was physically dispersed for 30 min by IKA dispersing machine and ultrasonically dispersed for 30 min until no obvious solid residue. In the glove box, the Li foil was cut into 12 cm and placed on a heating table at 150° C. Next, 2.5 mL FCNTs dispersion was taken into the spray gun and sprayed on the Li foil with 5 cm high. Finally, when the solvent on the surface of Li foil was evaporated completely, the FCNTs@Li anode was obtained.

2.2 Material characterization

Li metal is extremely reactive with H_2O and O_2 in the air. Therefore, all testing samples were disassembled in the glove box with H_2O and O_2 contents below 0.01 ppm (parts per million) and transferred through a sealed container to ensure the measurement accuracy. The obtained Li foil was cleaned with methoxymethane (DME) several times and naturally dried before characterization. The Li metal deposition was subjected to the morphology by field emission SEM (GeminiSEM 500). The surface state position of the Li metal was characterized by X-ray photoelectron spectroscopy (XPS, Escalab Xi^+). The time-of-flight secondary ion mass spectrometry (TOF-SIMS) surface spectra were tested at ion species of Bi^{3+} and energy of 30 keV in the high mass resolution mode. Meanwhile, the surface state position of the Li metal was etched by an Ar ion gun at 100 nA. The surface roughness of the Li metal anode was tested by an atomic force microscopy (AFM, SPM 5500, Keysight Technologies) inside an Ar-filled glove box. The optical photos of Li metal deposition were captured by a metallographic microscope (CX40M).

2.3 Electrochemical measurement

The CR2016 coin cells were selected for the full cell test, symmetry cell test, electrochemical impedance measurement, and Tafel slope test. For preparation of electrolyte, 1 mol L^{-1} $LiPF_6$ was dissolved in mixed solvent of ethylene carbonate (EC) and dimethyl carbonate (DMC) (1:1 by volume), and 10% mass content fluoroethylene carbonate (FEC) was added as an additive to stabilize the Li metal SEI. The NCM811 material was selected as the cathode in the full cell test. The loading mass of NCM811 cathodes was varied for different test conditions. When it was low, the NCM811 cathodes were made by mixing the NCM811 cathode material, acetylene black, and PVDF in a mass ratio of 8:1:1, added with appropriate NMP to form a slurry. The high-mass loading NCM811 electrode pieces were prepared with the same materials in the mass ratio of 94:3:3. Then, the slurry was coated on the cleaned aluminum foil, dried in an oven at 60°C for 24 h, and finally rounded into 11 mm diameter discs for future use. After weighing, the mass loading in the two cases were measured as 2.8 and 16.12 mg cm^{-2}, respectively. In the symmetry cell test, the Li foil was tested as both the working electrode and counter electrode, and 100 μL of electrolyte was consumed. The above cell tests were performed on the Neware battery cycler (Shenzhen, China).

The lithium-ion transference number (LTN) was investigated on an Autolab electrochemical workstation. The LTN test was measured using the steady-state current method, in which the electrochemical impedance spectroscopy (EIS) was tested before and after the chronoamperometry. The value of LTN was calculated by the equation as follows:

$$\mathrm{LTN} = \frac{I_S(V - I_0R_0)}{I_0(V - I_SR_S)}, \quad (1)$$

where R_0 and R_S represented the impedance before and after DC polarization, respectively; and I_0 and I_S referred to the initial and stable current during the polarization, respectively.

2.4 Pouch cell assembly

In this work, copper mesh, Celgard 2400, and NCM811 electrode provided by Tianjin Gateway Power Industry were selected as the anode current collector, separator, and cathode, respectively. First, the Li belt and copper mesh were simply rolled manually in an argon-filled glove box, and then placed into the prepared aluminum plastic film for heat sealing. Then, the pressed Li belt was placed into the glove box. After that, the Li belt, separator, and NCM811 electrode were stacked in sequence and moved into the aluminum plastic films. After added with electrolyte, they were treated with the heated sealer for a second seal to complete the entire pouch cell assembly. The assembled pouch cell was placed into the test system and subjected to the constant current and constant voltage discharge at 0.1 C rate and constant current charge at 0.1 C rate for 5 cycles to complete the formation. After that, the electrolyte reaction generated some gas in the pouch cell, and the airbag was inserted with a needle connected with a pump to suck the gas away.

2.5 Theoretical calculations

The Vienna *Ab-initio* Simulation Package (VASP) and the density functional theory (DFT) were employed in the theoretical calculations of this work. The exchange energy function was described using the Generalized Gradient Approximation (GGA) and the Perdew-Burke-Ernzerhof (PBE) functions. The near-nuclear electron wavefunction was described using the Projector Augmented Wave (PAW) pseudopotential method. The DFT+D3 was adopted to correct the dispersion interaction. The cutoff energy of the plane wave basis set was defined as 500 eV. The structure relaxations of LiF, Li_2O, and Li_2CO_3 with LiF-Li, Li_2O-Li, and Li_2CO_3-Li were optimized using the conjugate gradient method. Electron relaxation stopped until the change in total free energy was less than 1.0×10^{-5} eV, and the ion relaxation stopped until that of

its force was less than 0.02 eV $Å^{-1}$. A vacuum layer (12 Å thick) was added in the *Z*-axis direction for the slab models of LiF, Li_2O, and Li_2CO_3 to eliminate the mutual influence of adjacent periodic structures. A Gamma *k*-points mesh was set to be 6×6×1. A dipole correction was added in the *Z*-axis direction to correct the surface dipole. The density of states (DOS) of LiF, Li_2O, and Li_2CO_3 were calculated by the tetrahedral method. The adsorption energy was calculated with below equation:

$$E_{\mathrm{abs}} = E_{\mathrm{slab-Li}} - E_{\mathrm{slab}} - \frac{E_{\mathrm{Li}}}{2}, \quad (2)$$

where E_{abs} denoted the calculated adsorption energy, $E_{\mathrm{slab\text{-}Li}}$ referred to the total energy of Li adsorption on the compound slab model, E_{slab} indicated the total energy of compound slab model, and E_{Li} represented the total energy of the Li unit cell.

The electron-ion interactions were described by the PAW potentials, while the exchange-correlation interactions were calculated by employing the PBE pseudopotentials of GGA. Meanwhile, the vdW-D3 method developed by Grimme was employed to describe the van der Waals interaction. The plane-wave energy cutoff was set as 520 eV, and the convergence threshold was set as 1.0×10^{-5} eV in energy and 0.02 eV $Å^{-1}$ in force. The Brillouin zone was modeled by gamma centered Monkhorst-Pack scheme, in which a 0.04 $Å^{-1}$ grid was set for all models. The interface energy was evaluated using the same method by referring to a previous work. In addition, the lattice parameter perpendicular to the interface was relaxed while the others were fixed to optimize the interface configuration.

3. Results and discussion

3.1 Morphology characterization of FCNTs@Li electrode

Slurry coating using the doctor blade or blade coater is the most used to construct protective layers on the Li^0 metal surface [19-22]. However, its modification effectiveness under high-rate

cycling conditions is in doubt as the artificial SEI fabricated by such simple coating approaches is generally thick and nonuniform. In this work, a thin and uniform coating layer composed of FCNTs and PAMPS-Li is introduced on metallic Li^0 surface through spray coating (Fig. 1c) and is transformed to a multifunctional heterostructure SEI rich in LiF and PAMPS-Li by in-situ lithiation during cycling (Fig. 1d). In such a rational design, the nano-sized FCNTs could generate abundant crystalline LiF (< 10 nm) in the layer during the lithiation [23]. In the meantime, the single ion conductor PAMPS-Li (Fig. S1 online) with a bulky cross-linked structure (Fig. S2 online) remains as the binder in the SEI to act as the main organic components [24]. The uniform distribution of different elements confirms the successful construction of a homogeneous artificial SEI layer on metallic Li foil (Fig. S3 online). As a proof of concept, a simple synthesis platform was built in a glove box to verify the feasibility of the fabrication method in large-scale roll-to-roll projects, using a controllable motor as the power source and a heating machine instead of the industrial heating process (Fig. 1e). Finally, a roll of FCNTs@Li was obtained successfully through the simple self-built fabrication platform (Fig. 1f). As shown in Fig. 1g, the metallic Li^0 surface is homogenously covered by FCNTs without obvious exposure of Li^0 substrate. The cross-sectional SEM image (Fig. 1h) shows that t this coating layer is about 800 nm thick, which is in accordance with the expectation of artificial SEI. In addition, FCNTSs consume 1.045 mAh active Li in the first cycle for SEI construction (Fig. S4 online). Due to the 800 nm thickness, consumption ratio of FCNT to metallic Li can be calculated as 1.3 mAh mm^{-1}. Thus, FCNT does not consume too much active Li (0.05 mAh) in the 2rd–5th cycles. Therefore, it can be concluded that FCNT could not contribute much capacity during the subsequent cycling.

3.2 Electrochemical performance and Li deposition morphology

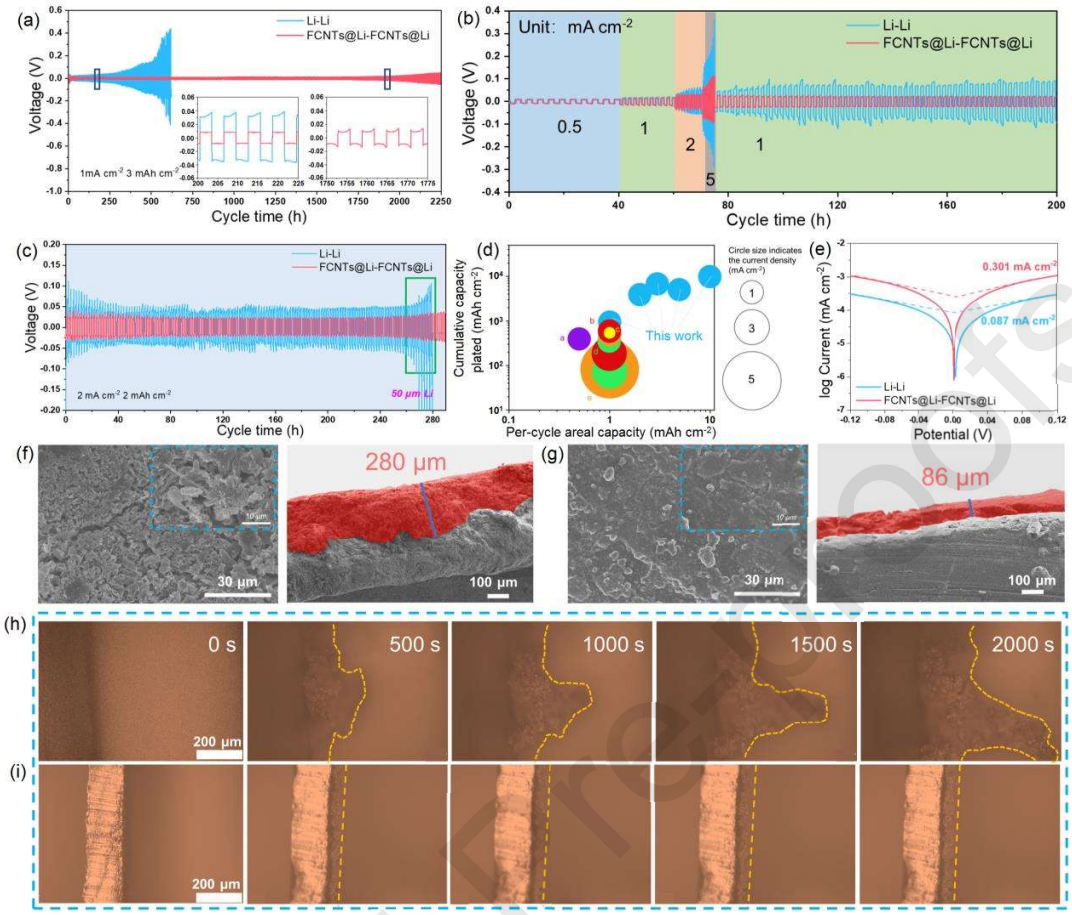

Fig. 2. (Color online) The electrode performance and metallic Li^0 deposition morphology images of FCNTs@Li. (a) The symmetry cell performance and zoomed-in images with current density of 1 mA cm^{-2} and deposition capacity of 3 mAh cm^{-2}. (b) The symmetry cell performance at different rates (0.5, 1, 2, and 5 mA cm^{-2}). (c) The symmetry cell performance when limited Li (50 μm thick) was applied. (d) The plot summarizing per-cycle areal capacity of the metallic Li^0 (*x*-axis), cumulative areal plating capacity (*y*-axis), and current density (size of each circle) in this work and analogous publications using ester electrolyte. Points and reference included: a) Ref. [27], b) Ref. [26], c) Ref. [28], d) Ref. [25], and e) Ref. [24]. (e) The Tafel plots of pure Li and FCNTs@Li. (f), (g) The front-section and cross-section SEM images of pure Li and FCNTs@Li after 50 cycles, respectively. (h), (i) *In situ* optical microscopy observation of

metallic Li^0 plating behavior of pure Li and FCNTs@Li with deposition rate of 0.5 mA cm^{-2}, respectively.

Galvanostatic metallic Li^0 plating/stripping test can identify the evolution and stability of the interface easily, as demonstrated in Fig. 2a−e. The current density for test is always set to 1 mA cm^{-2}. When the cycle capacity reached 1 mAh cm^{-2}, the metallic Li^0 without artificial SEI protection displayed a cycling overpotential near to 0.1 V in the initial stage of deposition, indicating that significant deposition energy barrier must be overcome. Moreover, the cycle overpotential climbs progressively and reaches 0.4 V after 400 hours of cycling (Fig. S5 online). Although there is no short-circuit caused by metallic Li^0 dendrite puncture, such huge energy loss can be termed cell failure. By contrast, FCNTs@Li initially exhibits a cycle overpotential of 0.05 V and can still maintain a stable cycle overpotential after th900 hours of cycling. Such finding suggests that FCNTs@Li can maintain a stable electrode interface for prolonged period, which is favorable to long-term deposition of metallic Li^0. The Figs. S6−S9 (online) demonstrate that the riding advantages provided by FCNTs@Li are increasingly noticeable as cycling capacity increases. In metallic Li^0 batteries, the areal capacity per cycle, the current density during plating/stripping, and the cumulative capacity of plated metallic Li^0 prior to short-circuit or cell failure are important parameters for evaluating cycling performance. The metallic Li^0 at low cycle capacity and cumulative capacity is far away from satisfying the actual application. Fig. 2d summarizes the recent publications which test the symmetry cell performance of metallic Li^0 using ester electrolyte. With a cumulative plating capacity of 6,750 mAh cm^{-2} (5000 and

10,000 mAh cm^{-2}), FCNTs@Li can cycle at huge areal capacities (up to 3, 5, and 10 mAh cm^{-2}), which greatly outperforms that of the mentioned publications, demonstrating the application of FCNTs@Li in metallic Li^0 batteries [25–30].

Since the diffusion speed of Li^+ in the electrolyte is faster than the migration speed in the SEI, the Li^+ will accumulate on the electrode surface, which can induce concentration polarization. The polarization overpotential may reflect the migration speed (speed step) of Li^+ on the electrode surface at greater current. FCNTs@Li exhibits superior performance than pure Li under various current densities (Fig. 2b), which is inextricably linked to the quicker transit speed of Li^+ on the FCNTs@Li interface (Fig. 2e). When enough excessive metallic Li^0 is furnished, Li^+ can be generated constantly, rendering the metallic Li^0 loss and side reaction in cycling unnoticeable [31–33]. When the metallic Li^0 for the metallic Li^0 plating/stripping is limited (thickness of 50 μm, equal to 10 mAh cm^{-2}), voltage of pure Li increases dramatically after 260 hours of cycling, revealing no active Li^0 accessible (Fig. S10 online). The FCNTs@Li owns fast Li^+ conduction and more stable interface, and exhibits outstanding advantage in symmetry cell tests at higher current densities and restricted metallic Li^0.

To thoroughly evaluate the impacts of SEI qualities on the morphologic features of metallic Li^0 deposition, the metallic Li^0 anode after 50 cycles were characterized (Fig. 2f). The cycled metallic Li^0 without FCNTs protection demonstrates an inhomogeneously disseminated porous structure, and the bulk of intact/dense metallic Li^0 remain in the cell. Consequently, the electrolyte is exhausted before the metallic Li^0 anode is destructed. Simultaneously, the insulating SEI layer rapidly enhances the cell resistance and accelerates the cell polarization, resulting in dramatic rise in overpotential after several cycles. A 280 μm-thick porous structure is formed by metallic Li^0 and SEI, approximately half of which remain pristine unbroken metallic

Li^0 after prolonged cycling, implying that the electrolyte is exhausted before Li^0 consumption. The sudden growth in the insulating SEI layer further exacerbates the surface electric field inhomogeneity, facilitating the uncontrolled development of metallic Li^0 dendrites (Fig. 2h). The comparison reveals that FCNTs@Li can remain the original anode structure (SEI/Li layer of 86 μm-thick, Fig. 2g), ensuring the protracted and even metallic Li^0 deposition (Fig. 2i). The titration gas chromatography (TGC) technique developed by Prof. Ying Shirley Meng was employed to monitor the metallic Li^0 on Li metal surface to characterize the inhibitory effect of FCNTs@Li more directly on inactive lithium (Fig. S11 online). When the hydrogen produced by the same mass of inactive lithium and water was measured using GC, we found that FCNTs@Li should significantly mitigate the growth of Li dendrites.

3.3 Calculation of interfacial energy and Li^+ binding energy

Journal Pre-proofs

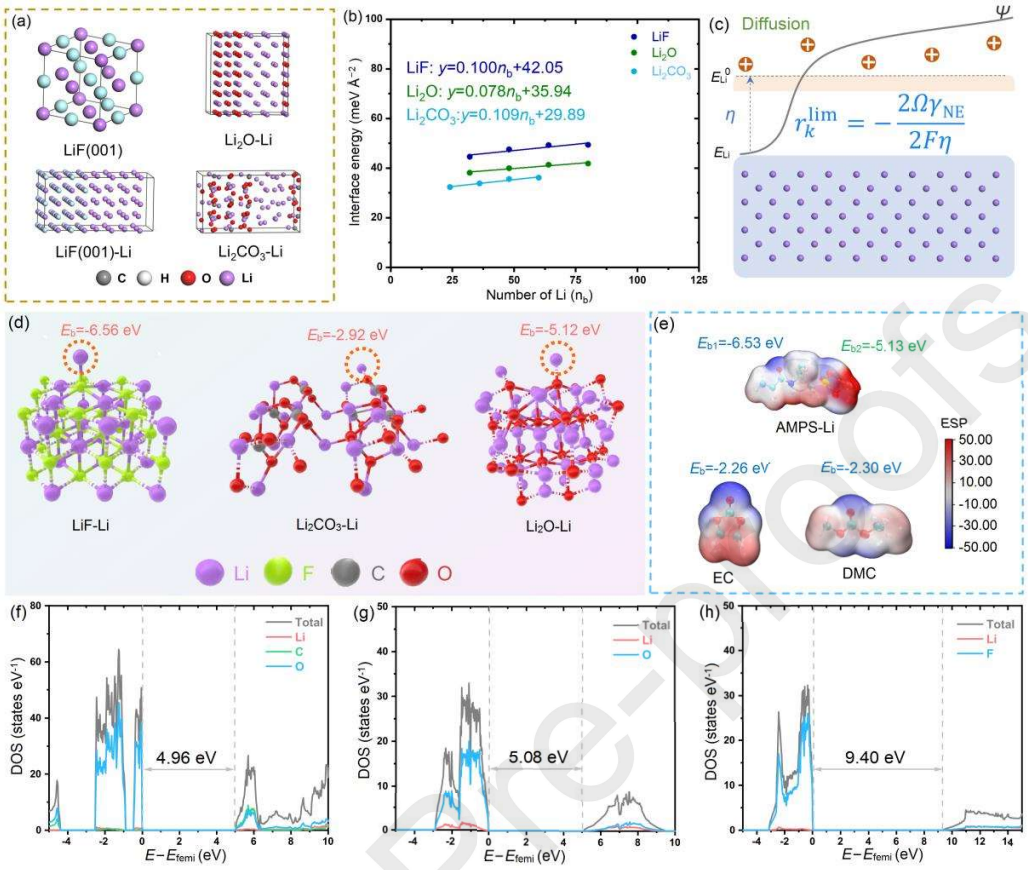

Fig. 3. (Color online) DFT calculations of the metallic Li^0 dendrite suppression mechanism by LiF-rich SEI formatted by FCNTs@Li. (a) Atomic structures of LiF (001) facet and heterojunctions with LiF-Li, Li_2O-Li, and Li_2CO_3-Li. (b) Relationship between interfacial energy of common inorganic components in SEI with lithium and the number of lithium units. (c) Graphical illustration on impacts of SEI's interfacial energy on metallic Li^0 deposition. (d) Absorption of Li^+ on the LiF, Li_2CO_3, and Li_2O. (e) Binding energy of Li^+ with different solvent molecules and organic components in SEI formatted by FCNTs@Li. (f), (g), and (h) The DOS profiles by atomic layer with Fermi level at 0 eV of Li_2CO_3, Li_2O, and LiF, respectively.

Journal Pre-proofs

Based on the DFT calculations, why LiF-rich SEI can effectively restrict the Li dendrites in Li metal batteries can be elucidated. Li_2CO_3 and Li_2O are mostly sourced from the unavoidable solvent reductive degradation in the EC/DMC system for $LiPF_6$. The results of blocking lithium dendrites were evaluated, and their heterojunction structures were constructed using LiF, Li_2CO_3, and Li_2O (Fig. 3a and Fig. S12 online) [34–36]. Since the Li^+ atoms develop perpendicular to the interface during the metallic Li^0 plating, the interfacial property for SEI is critical to the metallic Li^0 deposition. For coherent interfaces, the lattice planes are continuous at the interface, and the resulting interface structure can be described by a single periodic phase, which is set by the lattice constant of the composite system (defined as $\tilde{\Omega}$). Accordingly, interface between the two materials (defined as *a* and *b*) can be calculated with below equation (Note. S1 online):

$$\tilde{\gamma}_{ab}\left(\tilde{\Omega}, n_b\right) = \tilde{\gamma}_{ab}^{\lim}\left(\tilde{\Omega}\right) + n_b\sigma, \tag{3}$$

where σ was a constant related to the strain energy in material *b*. As assisted by Eq. (3), the interfacial energies of LiF, Li_2CO_3, and Li_2O were calculated (Tables S1−S3 and Fig. S13 online) [37–39]. Linear curves may be generated by computing the energies between different numbers of lithium units and lithium compounds. Intercept of the fitted linear curve represents the interfacial energy value between lithium and lithium compounds. Fig. 3b shows that LiF exhibits the greatest γ_{inter} of any binary lithium molecule (42.05 meV $Å^{-2}$), which is consistent with results of prior literature [40, 41]. According to the derivation method of R. Edwin Garc´ıa [42], the electroplating rate of metallic Li^0 is defined herein as below expression:

$$\Gamma = j_{\circ}\left(\exp\left[(1-\alpha)\left(\frac{zF\eta}{RT} + \frac{\gamma_{NE}\kappa\Omega}{RT}\right)\right] - exp\left[-\alpha\left(\frac{zF\eta}{RT} + \frac{\gamma_{NE}\kappa\Omega}{RT}\right)\right]\right), \tag{4}$$

where γ_{NE} was the interfacial energy of the metallic Li^0 surface, z referred to the valence of lithium ion, F represented the Faraday's constant, Ω stood for the Li^0 molar volume, and η denoted the electroplating overpotential. In addition, $j_\circ$, α, R, T, and κ represented the exchange current density, reaction symmetry factor, molar gas constant, absolute temperature, and curvature of the surface, respectively. Here, the interface contacted by the electrodeposited metallic Li^0 nucleus is the artificial heterostructure SEI. For the model of planar deposition that is routinely explored, Eq. (4) can evolve into one of the most basic kinetic relationships in electrochemistry, that is the Butler-Volmer equation:

$$\Gamma = j_\circ \left(\exp\left[(1-\alpha)\frac{zF\eta}{RT}\right] - \exp\left[-\alpha\frac{zF\eta}{RT}\right]\right). \quad (5)$$

In the case of small deviations from the equilibrium state, ($\frac{\gamma_{NE}\kappa\Omega}{RT} \ll 1$), and then the Eq. (4) above can be reduced as follows:

$$\Gamma = j_\circ \left(\frac{zF\eta}{RT} + \frac{\gamma_{NE}\kappa\Omega}{RT}\right). \quad (6)$$

The electrodeposition model for metallic Li^0 is usually a spherical model, with $v=\mathrm{d}r/\mathrm{d}t$ and $\kappa=2/r$. The growth rate of the nucleation size of Li^0 can be obtained by multiplying the interface deposition rate by the Li^0 molar volume, that is, $v=\Gamma\Omega$. Finally, the kinetic equation of Li^0 nucleation can be obtained as follows:

$$\frac{\mathrm{d}r}{\mathrm{d}t} = j_\circ\Omega \left(\frac{zF\eta}{RT} + \frac{2\gamma_{NE}\Omega}{rRT}\right). \quad (7)$$

Eq. (7) indicates that electrodeposition can also occur on the metallic Li^0 surface due to the presence of the interface, even without the effects of overpotential. Moreover, when derivative of the Li^0 nucleate size concerning time is 0, d*r*/d*t=0*, indicating that size of the Li^0 nucleus is no longer growing. At this time, the limit size of the Li^0 nucleation can be evolved as follows based on the Eq. (7):

$$r_k^{lim} = -\frac{2\gamma_{NE}\Omega}{zF\eta}. \quad (8)$$

If *z, F,* and *Ω* are set as constant values, the nucleate size of metallic Li^0 is proportional to the interface energy between SEI and lithium (Fig. 3c). Therefore, the LiF-rich SEI can attribute greater metallic Li^0 nucleate size and more stable metallic Li^0 deposition [43–45].

Compared with Li_2CO_3 (−2.92 eV) and Li_2O (−5.12 eV), the LiF-rich (−6.56 eV) heterostructure SEI presents the highest adsorption energy and a higher affinity for Li^+ (Fig. 3d). Thus, it forms several negative charge centers, which can pre-homogenize the Lewis acid Li^+ and facilitate the uniform Li^+ flux into the SEI [46]. The high insulation effect of SEI can thus delay the further reaction between the formed SEI and the electrolyte. The ability to transfer electrons from Li^+ to SEI is calculated directly from the DOS curve based on the difference between the conduction band minimum and the Fermi level (0 eV). LiF (9.40 eV, Fig. 3h) exhibits the highest band gap compared to Li_2CO_3 (4.96 eV, Fig. 3f) and Li_2O (5.08 eV, Fig. 3g), thus preventing further reactions with the electrolyte. Meanwhile, once the solvated Li^+ ions are transported to the SEI surface, the Li^+ will be desolvated and transported to the anode where it resides. The different positions of the monomers AMPS-Li (−6.53, −5.13 eV) exhibit higher binding energies to Li^+ than solvent molecules (EC, −2.26 eV; DMC, −2.30 eV), as illustrated in Fig. 3e.

Therefore, the solvated Li^+ can be rapidly desolvated at SEI formed by FCNTs@Li, thus hindering the parasitic reactions and accelerating the overall transition rate [47, 48].

3.4 Interface characterization and Li^+ desolvation

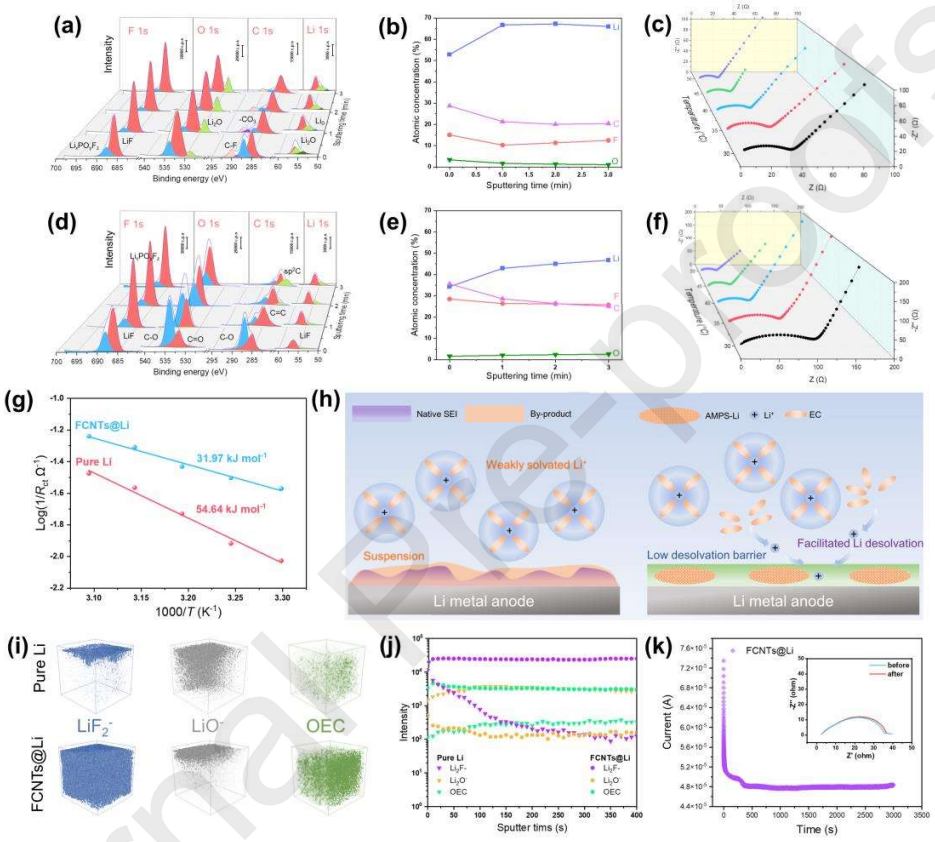

Fig. 4. (Color online) The SEI state analysis of metallic Li^0 surface after cycling. (a), (d) The C 1s, O 1s, F 1s, and Li 1s spectra of SEIs formed in pure Li and FCNTs@Li with different etching times, respectively. (b), (e) The changes in C, O, F and Li atomic concentrations with etching time in SEIs formed by pure Li and FCNTs@Li, respectively. (c) and (f) The EISs of pure Li and FCNTs@Li after the initial cycle at 30–50 °C, respectively. (g) The activation energy of symmetrical cells with pure Li and FCNTs@Li obtained from the Arrhenius formula. (h) Schematic illustration for desolvation of Li^+ on the pure Li (left) and FCNTs@Li (right). (i) The

TOF-SIMS depth profiles of SEIs film formed by pure Li and FCNTs@Li. (j) The depth distributions of Li_2F^-, LiO^-, and OEC with etching time in SEI film. (k) The *i-t* curves of chronoamperometry of the FCNTs@Li symmetry cell.

The generated SEI layer was subjected to the in-depth XPS to establish that it is endowed with LiF-rich nature by FCNTs@Li. The XPS spectra indicate the identical compositional peaks in the two SEI layers, which were $Li_xPO_yF_z$ (688.0 eV) and LiF (686.2 eV) in F 1s, C−O (533.8 eV) and C=O (531.5 eV) in O 1s, C−O (286.8 eV) and C=C (284.8 eV) in C 1s, and LiF (56.2 eV) and Li_2O (54.6 eV) in Li 1s (Fig. 4a, d) [49]. The proportion of Li_2O in the pure Li interface rapidly increases as the sputtering time. Due to lower oxidation potential, the Li ions are more prone to be accessible at the inner layer, resulting in more profoundly reactive Li_2O. Furthermore, pure Li exhibits a -CO_3 peak (288.8 eV) in C 1s, which typically corresponds to Li_2CO_3 in SEI and is formed by interaction of DMC with Li^+ in an endothermic process (Eq. (9)) but is not dispersed in FCNTs@Li [50].

$$CH_3OCO_2CH_3 + 2Li^+ + 2e^- + H_2 \rightarrow Li_2CO_3 + 2CH_4 \quad (9)$$

The peak intensity of Li_2O in pure Li is significantly higher than that in FCNTs@Li (the composition of Li_2O is not detected in O 1s due to very less content). The intensity of LiF is significantly lower than that of FCNTs@Li, indicating that LiF primarily involves in the SEI formation. The fluctuation of element atomic concentration with sputtering time (Fig. 4b, e)

demonstrates that the fluorine content in the SEI induced by FCNTs@Li is substantially greater (near to 30%, Fig. 4e) than that induced by the pure Li (10%−15%, Fig. 4b). The TOF-SIMS depth studies are carried out to acquire more about the composition of SEI (Fig. 4i, j) [51, 52]. After cycling, the major inorganic components (LiF_2^- and LiO^-) and organic species (oligo-ether carbonates) in SEI formed on the metallic Li^0 surface. It is evident that LiF_2^- in FCNTs@Li is evenly distributed across the dimension and possesses a substantially higher content than that in pure Li, while the content of LiO^- is very low in pure Li. In addition, the uniform distribution of CN^- in FCNTs@Li proves the high evenness of spray coating (Fig. S14 online). According to the theoretical calculation mentioned above, LiF with both high interfacial and binding energies with Li^+ can effectively promote the larger size of metallic Li^0 nucleation, which is advantageous for uniform metallic Li^0 deposition. According to previous research, PF_5^- may open the EC ring and realize ring-opening polymerization [53], which is consistent with the finding in this work (Fig. S15 online). When serving as an intermediate product, oligo-ether carbonate (OEC) possesses a longer carbon chain, so it is more flexibility than organic matters generated by EC just by opening the ring. During lithiation, the FCNTs@Li generates an abundance of PAMPS-Li, which can construct the Li ion channels, accelerating the ion transport within the interface and promoting the generation of OEC. Overall, the synergistic impacts of LiF with high interfacial and binding energies and OEC generation of longer segments in FCNTs@Li enhance the SEI that promotes uniform metallic Li^0 deposition and mitigates metallic Li^0 volume expansion, guaranteeing the highly stable cycling over time.

The activation energy (E_a) associated with activation barrier at the electrolyte/Li interface was calculated by fitting an equivalent circuit to the temperature dependence of the interface resistance, and the results are listed in Table S4 (online) [54]. At 30°C, the charge transfer

resistance (R_{ct}) of the FCNTs@Li is estimated to be 37.1 Ω (Fig. 4f and Fig. S16 online), which is substantially lower than that of pure Li (106.2 Ω, Fig. 4c). Such finding suggests that the FCNTs@Li interface is advantageous for Li^+ transportation, which agrees with result displayed by the Tafel curve. The E_a at the electrolyte/Li interface can be calculated using the Arrhenius equation, as follows:

$$\frac{1}{R_{ct}} = A\exp\left(-\frac{E_a}{RT}\right), \quad (10)$$

where A is a constant, R is the molar gas constant, and T is the absolute temperature. The calculated E_a of Li^+ desolvation in FCNTs@Li (31.97 kJ mol^{-1}) is lower than that in pure Li (54.64 kJ mol^{-1}), confirming that the interfacial layer generated by FCNTs@Li is favorable to separation of Li^+-solvated sheaths, allowing for faster Li^+ intercalation kinetics (Fig. 4g). The high absorption energies of -CONH and -SO_3 with Li^+ in AMPS-Li can facilitate the separation of Li^+-solvated sheaths at the interface layer (Fig. 3e). As previously reported, SEI with high LTN assist enhances the critical size of metallic Li^0 nucleation, smooth Li deposition, and diminish parasitic interactions of anions with metallic Li^0. The LTN values of FCNTs@Li and pure Li are estimated to be 0.66 and 0.33, respectively (Table S5 and Fig. S17 online). Due to Note S2 (online), the high LTN of FCNTs@Li enables ion transport and balance of surface tension, ultimately promoting the large size of metallic Li^0 nucleation [55]. FCNT+PVDF and PAMPS-Li+PVDF are selected and sprayed onto the Li foil separately for comparison to clarify the role of each component (Fig. S18 online). The sample with FCNT+PVDF can maintain low overpotential due to a LiF-dominated SEI interface, which is conductive to the Li^+ transport. However, the LiF-dominated SEI interface without organic component protection consumes amounts of active Li and is deactivated after long-term cycling. The sample with PAMPS-

Li+PVDF exhibit a larger overpotential due to poor ionic conductivity. As a result, the PAMPS-Li in FCNTs@Li can effectively suppress the anion migration, reducing the parasitic reactions and by-products (Fig. 4h).

3.5 Full-cell performance of coin cell and pouch cell with high-loading NCM811 cathode

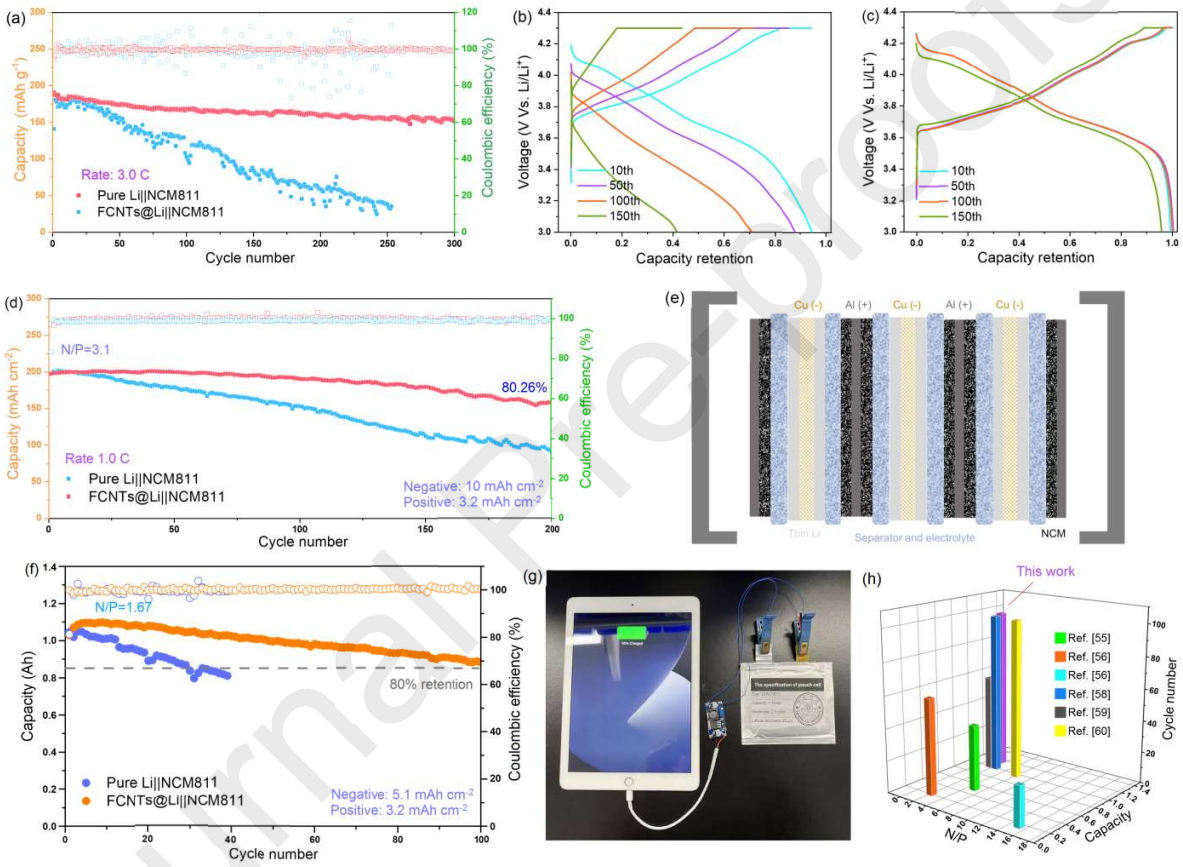

Fig. 5. (Color online) Comparison of NCM811 cull cell electrochemical performance in coin cell and pouch cell. (a) The NCM811 full cell electrochemical performance with the current density of 3.0 C (1.68 mA cm^{-2}). (b) and (c) The voltage-capacity retention curves of pure Li||NCM811 and FCNTs@Li||NCM811, respectively, during different cycles. The NCM811 full cell electrochemical performance with the current density of 1.0 C (3.2 mA cm^{-2}) involves high

loading NCM811 cathode (mass loading of 16.12 mg cm^{-2}, 3.2 mAh cm^{-2}) and limited Li metal anode (thickness of 50 μm, 10 mAh cm^{-2}), indicating that the N/P ratio is 3.1. (e) The definite structural relationship of the cathode electrode and anode electrode to the separator inside the Li metal pouch cell. (f) The NCM811 pouch cell electrochemical performance with the charge rates of 0.5 C (1.61 mA cm^{-2}) and 0.1 C (0.32 mA cm^{-2}). The embedded image is the optical photograph of assembled FCNTs@Li||NCM811 pouch cell with a capacity of 1.15 Ah. (g) Schematic diagram of Li metal pouch cell. (h) The plot for total capacities of the Li-metal pouch cell (*x*-axis), N/P ratio (*y*-axis), and the cycling number (*z*-axis) in this work and analogous publications assembled with lithium-containing cathodes (NCM or LFP).

The metallic Li^0 anode is combined with NCM811 cathode to assemble the full cells for electrochemical tests, aiming to illustrate the potential of FCNTs@Li under the actual situation. When the loading of NCM811 is 2.8 mg cm^{-2}, the applied current density is controlled at 1.68 mA cm^{-2} (3 C). The initial capacity of the FCNTs@Li||NCM811 full cell is 187.8 mAh g^{-1}, and the discharge specific capacity of 151.8 mAh g^{-1} (retention rate of 80.8%) still is maintained after 300 cycles (Fig. 5a, c, and Table S6 online). In contrast, the pure Li||NCM811 full cell exhibits a initial capacity of 180.9 mAh g^{-1} and decays rapidly after 50 cycles (Fig. 5b). The results discussed here indicate that interface of pure Li becomes progressively polarized when the SEI thickens and the amount of Li^0 in the insulating state grows, enhancing the Li^+ transport resistance and accelerating the capacity degradation. High-loading cathode, limited metallic Li^0 anode, and lean electrolyte must be applied concurrently to maximize the gravimetric energy density of metallic Li^0 batteries. The FCNTs@Li||NCM811 full cell maintains a capacity loss of only ~0.0987% per cycle (Fig. 5d) when it is assembled with high-loading NCM811 cathode

(mass loading of 16.12 mg cm^{-2}, 3.2 mAh cm^{-2}) and limited Li metal anode (thickness of 50 μm, 10 mAh cm^{-2}, N/P ratio of 3.1), and lean electrolyte (E/C ratio of 5 g Ah^{-1}) at the current density of 3.2 mA cm^{-2} (1 C). The capacity loss obviously exceeds the comparable state-of-the-art Li^0 metal anodes recently published (Fig. S19 online). The 'wet SEI' layers are generated when the FCNTs@Li metal surfaces are wetted by the electrolyte, leaving some residual electrolytes behind. As a result, Li^+ flux flows back and forth between these wetted SEI layers, realizing the electrochemical process.

In our perspective, the spray coating synthesis approach can swiftly generate the FCNTs@Li foil, making it ideal for pouch cell assembly. As a proof-of-principle, a multilayer laminated pouch cell was assembled with the N/P ratio of 1.67 (Table S7 and Fig. S20 online), and the precise structure is shown in the Fig. 5e. The FCNTs@Li||NCM811 pouch cell can supply a specific energy of 330 Wh kg^{-1} and support the stable cycle for 100 cycles at baseline capacity retention of 80% (Fig. 5f), whereas the pure Li||NCM811 pouch cell rapidly declines after 30 cycles (Fig. 5g). Compared with recent literature about pouch cell electrochemical performance [56–61], the pouch cells in this work can keep cycle stability for the longest time under severe conditions with higher gravimetric energy density (1.15 Ah) and lower N/P (1.67) (Fig. 5h). It demonstrates the long-term cycling stability of FCNTs@Li||NCM811 metallic Li^0 batteries under industrially practical harsh conditions.

4. Conclusion

In summary, a multifunctional artificial SEI is designed on metallic Li^0 via simple spray coating and in-situ lithiation process in this work, which can realize rapid desolvation of Li^+ and uniform metallic Li^0 deposition. DFT calculation results verify that LiF (001) facet owns higher

interfacial energy than other inorganic components (Li_2O and Li_2CO_3) in native SEI, so it can promote the metallic Li^0 deposition with larger nucleate size from. Besides, insulation of LiF in SEI can effectively suppress the formation of the metallic Li^0 dendrites. The PAMPS-Li can restrain the movement of anions in the SEI and promote the desolvation of Li^+, thus hindering the electrolyte penetration, mitigating the side reactions between Li^0 and electrolyte, and enhancing the metallic Li^0 nucleate size. As a proof of concept, a 330 Wh kg^{-1} metallic Li^0 pouch cell (N/P of 1.67) is implemented for 100 stable cycles assisted by the elf-built simple roll-to-roll production system. Therefore, it is believed that the strategy proposed in this work provides a novel direction for realizing large-scale production of high-performance metallic Li^0 anodes.

Conflict of interest

The authors declare that they have no conflict of interest.

Acknowledgments

This work was supported by the National Natural Science Foundation of China (22109030 and 21875195), Guangdong Basic and Applied Basic Research Foundation (2019A1515111069 and 2021A1515010177), and The Key Research and Development Program of Yunnan Province (202103AA080019). The author also thanks the figure platform provided by Figdraw. We are grateful to the Tan Kah Kee Innovation Laboratory (IKKEM) for help with XPS, SEM.

Journal Pre-proofs

Author Contributions

Zhipeng Wen performed the experiment, conducted materials characterizations, analyzed the data, and wrote the draft of the manuscript. Yuanhong Kang contributed to the computation and data analysis. Qilong Wu, Xiu Shen, and Pengbin Lai performed materials characterizations and data analysis. Yang Yang, Cheng Chao Li, and Jinbao Zhao contributed for the result discussion and manuscript writing. All authors approved the final version of the manuscript.

References

[1] D.C. Lin, Y.Y. Liu, Y. Cui. Reviving the lithium metal anode for high-energy batteries. Nat Nanotechnol. 2017; 12: 194–206.

[2] S. Jin, Y. Jiang, H.X. Ji, et al. Advanced 3D current collectors for lithium-based batteries. Adv Mater 2018; 30: e1802014.

[3] G.W. Chen, Z.L. Gong. Study on Li_3BO_3 interface modification of garnet solid electrolyte. J Electrochem, 2021; 27: 76–82.

[4] C. Fang, J. Li, M. Zhang, et al. Quantifying inactive lithium in lithium metal batteries. Nature 2019; 572: 511–515.

[5] Y. Yang, J. Xiong, S.B. Lai, et al. Vinyl ethylene carbonate as an effective SEI-forming additive in carbonate-based electrolyte for lithium-metal anodes. ACS Appl Mater Interfaces 2019; 11: 6118–6125.

Journal Pre-proofs

[6] X.R. Chen, B.Q. Li, C. Zhu, et al. A coaxial-interweaved hybrid lithium metal anode for long‐lifespan lithium metal batteries. Adv Energy Mater 2019; 9: 1901932.

[7] Z.P. Wen, Y.Y. Peng, J.L. Cong, et al. A stable artificial protective layer for high capacity dendrite-free lithium metal anode. Nano Res 2019; 12: 2535–2542.

[8] L.S. Fan, B. Sun, K. Yan, et al. A dual-protective artificial interface for stable lithium metal anodes. Adv. Energy Mater. 2021; 11: 2102242.

[9] L. Fan, H.L. Zhuang, W.D. Zhang, et al. Stable lithium electrodeposition at ultra-high current densities enabled by 3D PMF/Li composite anode. Adv Energy Mater 2018; 8: 1703360.

[10] F. Liu, R. Xu, Y.C. Wu, et al. Dynamic spatial progression of isolated lithium during battery operations. Nature 2021; 600: 659–663.

[11] D. Wang, C. Qin, X. Li, et al. Synchronous healing of Li metal anode via asymmetrical bidirectional current. iScience 2020; 23: 100781.

[12] Z.J. Ju, G.X. Lu, O.W. Sheng, et al. Soybean protein fiber enabled controllable Li deposition and a LiF-nanocrystal-enriched interface for stable Li metal batteries. Nano Lett 2022; 22: 1374–1381.

[13] G. Li, S. Liu, Z. Liu, et al. High interfacial-energy and lithiophilic janus interphase enables stable lithium metal anodes. Small 2021; 17: e2102196.

[14] S.F. Liu, X.H. Xia, S.J. Deng, et al. *In situ* solid electrolyte interphase from spray quenching on molten Li: a new way to construct high-performance lithium-metal anodes. Adv Mater 2019; 31: e1806470.

Journal Pre-proofs

[15] Y.J. Liu, X.Y. Tao, Y. Wang, et al. Self-assembled monolayers direct a LiF-rich interphase toward long-life lithium metal batteries. Science 2022; 375: 739–745.

[16] Y.S. Li, K. Leung, Y. Qi. Computational exploration of the Li-electrode|electrolyte interface in the presence of a nanometer thick solid-electrolyte interphase layer. Acc Chem Res 2016; 49: 2363–2370.

[17] H. Liu, X.B. Cheng, J.Q. Huang, et al. Controlling dendrite growth in solid-state electrolytes. ACS Energy Lett 2020; 5: 833–843.

[18] Q. Zhao, S. Stalin, L.A. Archer. Stabilizing metal battery anodes through the design of solid electrolyte interphases. Joule 2021; 5: 1119–1142.

[19] J. Luo, C.C. Fang, N.L. Wu. High polarity poly(vinylidene difluoride) thin coating for dendrite-free and high-performance lithium metal anodes. Adv Energy Mater 2018; 8: 1701482.

[20] Y. Liu, D. Lin, P.Y. Yuen, et al. An artificial solid electrolyte interphase with high li-ion conductivity, mechanical strength, and flexibility for stable lithium metal anodes. Adv Mater 2017; 29: 1605531.

[21] M.G. Zhu, Z.C. Fan, K.L. Xu, et al. An oxygen-resistant and self-eliminating passivated layer for highly stable lithium metal batteries. Adv Funct Mater 2022; 32: 2112645.

[22] C. Chen, Q.W. Liang, Z.X. Chen, et al. Phenoxy radical-induced formation of dual-layered protection film for high-rate and dendrite-free lithium-metal anodes. Angew Chem Int Ed, 2021; 60: 26718–26724.

Journal Pre-proofs

[23] B. Sayahpour, H. Hirsh, S. Bai, et al. Revisiting discharge mechanism of CFx as a high energy density cathode material for lithium primary battery. Adv Energy Mater 2021; 12: 2103196.

[24] X. Shen, L.Q. Peng, R.Y. Li, et al. Semi-interpenetrating network-structured single-ion conduction polymer electrolyte for lithium-ion batteries. ChemElectroChem 2019; 6: 4483–4490.

[25] J.H. You, H.T. Deng, X.M. Zheng, et al. Stabilized and almost dendrite-free Li metal anodes by *in situ* construction of a composite protective layer for Li metal batteries. ACS Appl Mater Interfaces 2022; 14: 5298–5307.

[26] J. Lee, M. Shin, D.K. Hong, et al. Efficient li-ion-conductive layer for the realization of highly stable high-voltage and high-capacity lithium metal batteries. Adv Energy Mater 2019; 9: 1803722.

[27] Q.S. Xu, J.J. Lin, C.C. Ye, et al. Air-stable and dendrite-free lithium metal anodes enabled by a hybrid interphase of C60 and Mg. Adv Energy Mater 2019; 10: 1903292.

[28] D. Wu, J. He, J. Liu, et al. Li_2CO_3/LiF−rich heterostructured solid electrolyte interphase with superior lithiophilic and Li^+−transferred characteristics via adjusting electrolyte additives. Adv Energy Mater 2022; 12: 2200337.

[29] S. Han, Z. Li, Y. Zhang, et al. *In-situ* formation of a nanoscale lithium aluminum alloy in lithium metal for high-load battery anode. Energy Storage Mater 2022; 48: 384–392.

[30] C.P. Yang, H. Xie, W.W. Ping, et al. An electron/ion dual-conductive alloy framework for high-rate and high-capacity solid-state lithium-metal batteries. Adv Mater 2019; 31: e1804815.

[31] X.D. Lin, Y. Gu, X.R. Shen, et al. An oxygen-blocking oriented multifunctional solid–electrolyte interphase as a protective layer for a lithium metal anode in lithium-oxygen batteries. Energy Environ Sci 2021; 14: 1439–1448.

[32] P. Xu, X.D. Lin, X.Y. Hu, et al. High reversible Li plating and stripping by *in-situ* construction a multifunctional lithium-pinned array. Energy Storage Mater 2020; 28: 188–195.

[33] P. Xu, X.D. Lin, Z.Q. Sun, et al. A robust interphase via *in-situ* pre-reconfiguring lithium anode surface for long-term lithium-oxygen batteries. J Energy Chem 2022, 72：186-194

[34] F.H. Ren, Z.D. Li, L.Y. Huai, et al. High-loading lateral Li deposition realized by a scalable fluorocarbon bonded laminates. Carbon 2021; 171: 894–906.

[35] T.R. Wang, J. Duan, B. Zhang, et al. A self-regulated gradient interphase for dendrite-free solid-state Li batteries. Energy Environ Sci 2022; 15: 1325–1333.

[36] X.L. Fan, J. Xiao, F.D. Han, et al. Fluorinated solid electrolyte interphase enables highly reversible solid-state Li metal battery. Sci Adv 2018; 4: eaau9245.

[37] N.D. Lepley, N.A.W. Holzwarth. Modeling interfaces between solids: Application to Li battery materials. Phys Rev B 2015; 92: 214201.

[38] J.S. Lowe, D.J. Siegel. Modeling the interface between lithium metal and its native oxide. ACS Appl Mater Interfaces 2020; 12: 46015–46026.

[39] K. Leung, F. Soto, K. Hankins, et al. Stability of solid electrolyte interphase components on lithium metal and reactive anode material surfaces. J Phys Chem C 2016; 120: 6302–6313.

[40] H. Su, Y. Liu, Y. Zhong, et al. Stabilizing the interphase between Li and argyrodite electrolyte through synergistic phosphating process for all-solid-state lithium batteries. Nano Energy 2022; 96: 107104.

[41] R.C. Xu, F.D. Han, X. Ji, et al. Interface engineering of sulfide electrolytes for all-solid-state lithium batteries. Nano Energy 2018; 53: 958–966.

[42] D.R. Ely, R.E. García. Heterogeneous nucleation and growth of lithium electrodeposits on negative electrodes. J Electrochem Soc 2013; 160: A662–A668.

[43] J. Lopez, A. Pei, J.Y. Oh, et al. Effects of polymer coatings on electrodeposited lithium metal. J Am Chem Soc 2018; 140: 11735–11744.

[44] P. Biswal, S. Stalin, A. Kludze, et al. Nucleation and early stage growth of Li electrodeposits. Nano Lett 2019; 19: 8191–8200.

[45] A. Pei, G.Y. Zheng, F.F. Shi, et al. Nanoscale nucleation and growth of electrodeposited lithium metal. Nano Lett 2017; 17: 1132–1139.

[46] Y. Yu, G. Huang, J.Z. Wang, et al. *In situ* designing a gradient Li^+ capture and quasi-spontaneous diffusion anode protection layer toward long-life Li-O2 batteries. Adv Mater 2020; 32: e2004157.

[47] M.S. Kim, Z. Zhang, P.E. Rudnicki, et al. Suspension electrolyte with modified Li^+ solvation environment for lithium metal batteries. Nat Mater 2022; 21: 445-454.

[48] Y.C. Wen, J.Y. Ding, Y. Yang, et al. Introducing NO_3^- into carbonate-based electrolytes via covalent organic framework to incubate stable interface for Li-metal batteries. Adv Funct Mater 2021; 32: 2109377.

[49] Y.H. Tan, G.X. Lu, J.H. Zheng, et al. Lithium fluoride in electrolyte for stable and safe lithium-metal batteries. Adv Mater 2021; 33: e2102134.

[50] P. Verma, P. Maire, P. Novak. A review of the features and analyses of the solid electrolyte interphase in Li-ion batteries. Electrochimica Acta 2010; 55: 6332–6341.

[51] B. Xu, X. Li, C. Yang, et al. Interfacial chemistry enables stable cycling of all-solid-state Li metal batteries at high current densities. J Am Chem Soc 2021; 143: 6542–6550.

[52] K. Zhang, W. Liu, Y.L. Gao, et al. A high-performance lithium metal battery with ion-selective nanofluidic transport in a conjugated microporous polymer protective layer. Adv Mater 2021; 33: e2006323.

[53] M. Moshkovich, M. Cojocaru, H.E. Gottlieb, et al. The study of the anodic stability of alkyl carbonate solutions by *in situ* FTIR spectroscopy, EQCM, NMR and MS. J Electroanal Chem 2001; 497: 84–96.

[54] Y. Yang, H. Zhu, F. Yang, et al. Ten thousand-cycle ultrafast energy storage of wadsley-roth phase Fe-Nb oxides with a desolvation promoting interfacial layer. Nano Lett 2021; 21: 9675–9683.

[55] M.D. Tikekar, S. Choudhury, Z.Y. Tu, et al. Design principles for electrolytes and interfaces for stable lithium-metal batteries. Nat Energy 2016; 1: 1–7.

Journal Pre-proofs

[56] C.B. Jin, T.F. Liu, O.W. Sheng, et al. Rejuvenating dead lithium supply in lithium metal anodes by iodine redox. Nat Energy 2021; 6: 378–387.

[57] S.Y. Li, S.C. Zhang, S.Y. Chai, et al. Structured solid electrolyte interphase enable reversible Li electrodeposition in flame-retardant phosphate-based electrolyte. Energy Storage Mater 2021; 42: 628–635.

[58] Z.P. Wen, H. Li, H.Y. Li, et al. Highly stable and robust bi-electrodes interfacial protective films for practical lithium metal batteries. J Power Sources 2021; 509: 230370.

[59] J.Y. Chen, S.J. Li, X. Qiao, et al. Integrated porous Cu host induced high-stable bidirectional Li plating/stripping behavior for practical Li metal batteries. Small 2022; 18: e2105999.

[60] P. Shi, Z.Y. Liu, X.Q. Zhang, et al. Polar interaction of polymer host-solvent enables stable solid electrolyte interphase in composite lithium metal anodes. J Energy Chem. 2022; 64: 172–178.

[61] Q. Zhao, N.W. Utomo, A.L. Kocen, et al. Upgrading carbonate electrolytes for ultra-stable practical lithium metal batteries. Angew Chem Int Ed 2022; 61: e202116214.

Zhipeng Wen[1,2], Yuanhong Kang[2], Qilong Wu[2], Xiu Shen[2], Pengbin Lai[2], Yang Yang[2*], Cheng Chao Li[1*], Jinbao Zhao[2*]

Journal Pre-proofs

Zhipeng Wen received his Bachelor's degree from Hunan University in 2017 and Ph.D. degree in Physical Chemistry from Xiamen University in 2022. He is currently a postdoctoral fellow in the research group of Prof. Cheng Chao Li at Guangdong University of Technology. His research focuses on aqueous zinc-ion batteries and high energy Li metal batteries.

Yang Yang received his Bachelor's degree from Northeastern University in 2009 and Ph.D. degree in Applied Chemistry from Xiamen University in 2018. He is currently an associate professor at Xiamen University. His research focuses on aqueous zinc-ion batteries, high-safety Wadsley-Roth phase electrode materials, and *in situ* electrochemical characterization techniques.

Journal Pre-proofs

Cheng Chao Li is currently a professor at the School of Chemical Engineering and Light Industry, Guangdong University of Technology. He received his Ph.D. degree from the School of Materials Science & Engineering, Hunan University in 2013. From 2008 to 2012, he was supported by CSC to conduct his research on nanomaterials synthesis and self-assembly as an exchange Ph.D. student in Prof. Hua Chun Zeng's group at National University of Singapore. His research interest includes the synthesis of advanced electrode materials and design of multifunctional electrode interfaces in aqueous rechargeable batteries.

Jinbao Zhao received his Bachelor's degree from Harbin Institute of Technology in 1984 and Ph.D. degree in Polymer Chemistry from Kyoto University in 1996. He worked as a senior

Journal Pre-proofs

researcher at the Hitachi Research Lab for more than 12 years. He is currently a professor at Xiamen University. His research topic includes chemical energy storage systems and related materials. He specializes in the basic research and technological development of lithium-ion batteries with high energy density and fuel cells.

Graphic abstract

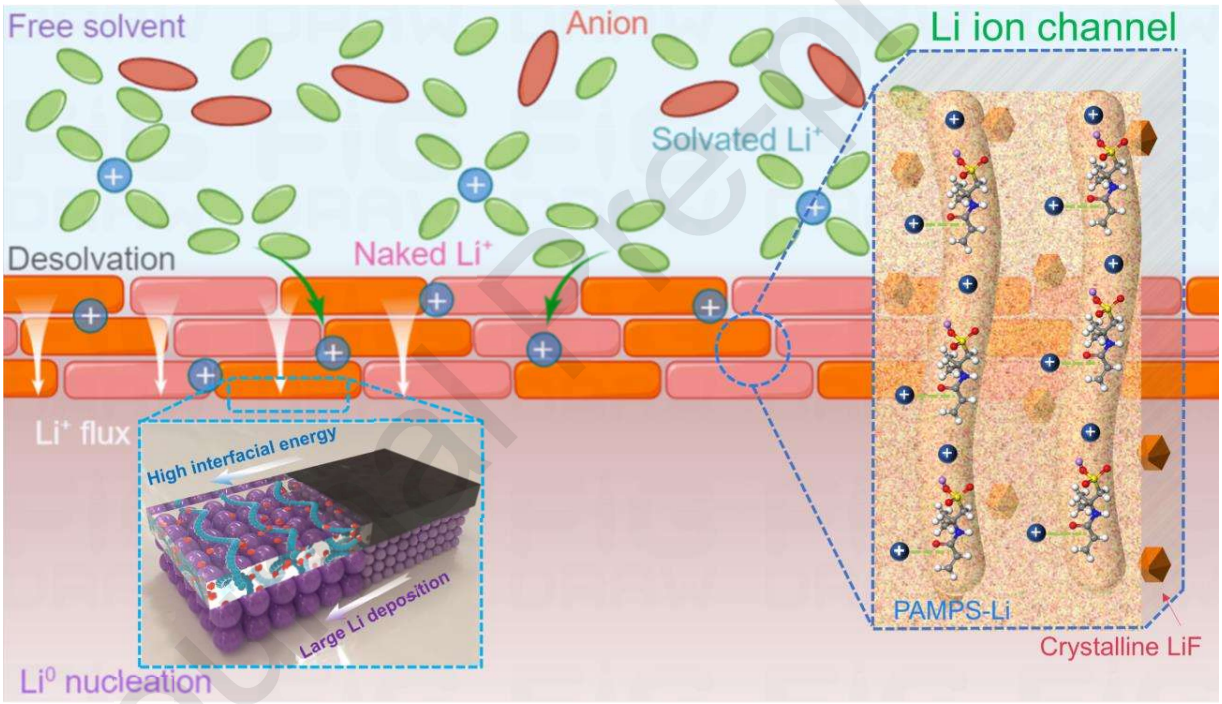

Based on the in-depth understanding of Li^0 deposition behavior, a high interfacial-energy artificial SEI with rich LiF embedded in PAMPS-Li polymer network is designed to realize favorable Li^0 nucleation and rapid desolvation of Li^+ simultaneously, reveals the importance of interfacial energy for highly reversible Li^0 deposition/stripping.

Journal Pre-proofs